A Study on the Crystalline Structure of Sodium Titanate Nanobelts Prepared by the Hydrothermal Method

Dong Ri Zhang,[‡] Chang Woo Kim,[†] and Young Soo Kang*,[†]

Department of Chemistry, Sogang University, Seoul 121-742, South Korea, and Department of Chemical Engineering and Polymer Science, College of Engineering, Yanbian University, Yanji 133002, China

Received: February 18, 2010; Revised Manuscript Received: April 1, 2010

The formation and crystal structure of sodium titanate nanobelts synthesized with various Ti precursors are reported. P25 (TiO_2) powder, $Ti(OBu)_4$, and $TiCl_4$ were used as Ti precursors. Their nanobelts were synthesized via hydrothermal process at 180 °C for 24 h in concentrated aqueous NaOH solution. The product obtained with P25 (TiO_2) was identified to be $Na_2Ti_4O_9 \cdot 1.5H_2O$. The products obtained with $Ti(O(CH_2)_3CH_3)_4$ and $TiCl_4$ were confirmed to be the crystal structure of $Na_2Ti_2O_4(OH)_2$. This means that the formation mechanism of the crystal structure in the synthetic process depends on their Ti source. Their morphology was compared with XRD, TEM, FE-SEM, Raman, and TGA. On the basis of their morphology results, the crystalline structure model and the formation mechanism of sodium titanate nanobelts are proposed.

Introduction

Since the first report[1] on TiO_2 nanotubes which were synthesized via the hydrothermal process under aqueous NaOH solution, there has been intensive research on the growth mechanism and crystalline structure of one-dimensional nanosized TiO_2[2–6] and various titanate nanomaterials[7–17] because of their potential applications in many fields such as photocatalysis,[7,18] solar energy conversion,[19] and sensors.[20] Recently, there have been many reports on the synthesis and characterization of one-dimensional alkali metal titanate nanomaterials owing to their size and shape-dependent optical properties.[11,12,21–25] It has been reported that the structures of these titanates are built from a sheet characterized by edge- and/or corner-sharing of TiO_6 octahedra, which forms a zigzag ribbon or tunnel structures.[26] As a photocatalyst, these structures are suitable for the accommodation of the catalytic active phases such as noble metal atoms which work to enhance the efficiency of the separation of photoexcited charges (i.e., electron and hole) and also for their transfer to adsorbed reactants at the surface. Thus, it would be expected that these titanates become promising photocatalytic materials. Among various alkali metal titanate nanomaterials, sodium titanate is of particular interest for its wide applications, such as high photocatalytic activities,[23] ion-exchange ability,[24] and photovoltaic characteristics.[25]

It is well-known that the chemical composition of the products obtained through the hydrothermal synthesis in a concentrated aqueous NaOH solution is very sensitive due to their washing process. As such, the exact chemical composition of the products is fussy to determine. On the other hand, the hydrothermal process displays in general one-dimensional morphology, such as nanotubes, nanowires, nanorods, and nanobelts. Considering these situations, many hypotheses have been proposed to determine the exact crystalline structure of the products and explain the formation mechanism of the morphologies of the products.[6–9,12,16] In this study, we report the synthesis of sodium titanate nanobelts via the hydrothermal method in a concentrated aqueous NaOH solution using three different precursors. The synthesized products were characterized by X-ray powder diffraction (XRD), high-resolution transmission electron microscopy (HRTEM), selected area electron diffraction (SAED), field emission scanning electron microscopy (FE-SEM), Raman spectroscopy, and thermogravimetric analysis (TGA) measurements. On the basis of the results, the crystalline structure model and the formation mechanism of sodium titanate nanobelts are proposed.

Experimental Section

Synthesis of Sodium Titanate Nanobelts. Titanium(IV) butoxide ($Ti(OBu)_4$, 97+%), titanium(IV) chloride ($TiCl_4$, 99.9%), and absolute ethyl alcohol (C_2H_5OH, 99.9%) were obtained from Aldrich Chemical Co. and titanium dioxide powder (P25) was purchased from Degussa Corp. (Germany), respectively, and used as received. In these experiments, three different compounds of TiO_2 (P25) powder, titanium(IV) butoxide ($Ti(OBu)_4$), and titanium(IV) chloride ($TiCl_4$) were used as Ti precursors and 10 M NaOH aqueous solution was used as the solvent. A set of acronyms is used for all samples: TP, TB, and TC denote the synthesized samples using TiO_2 (P25), titanium(IV) butoxide, and titanium(IV) chloride as the Ti precursors, respectively. For TP, 600 mg of P25 was dispersed in 40 mL of 10 M aqueous NaOH solution in a Teflon vessel and the solution was moved into an autoclave, then heated in a furnace at 180 °C for 24 h. After cooling, the final product was filtered and washed with deionized water several times. The product was dried at room temperature freely. For TB, 2 mL of $Ti(OBu)_4$ was added into 20 mL of a C_2H_5OH solution and then the solution was mixed with 20 mL of a 10 M aqueous NaOH solution in a Teflon vessel. For TC, 1 mL of $TiCl_4$ was added into 40 mL of a 10 M aqueous NaOH solution in a Teflon vessel. The following procedures are the same as mentioned above. To explore the thermal stability of the crystal structure of the products, the three as-synthesized samples were calcined at 500 °C for 6 h and they are in turn denoted as TP-500, TB-500, and TC-500, respectively.

* To whom correspondence should be addressed. Phone: + 82 2 705 8882. Fax: + 82 2 701 0967. E-mail: yskang@sogang.ac.kr.
‡ Yanbian University.
† Sogang University.

10.1021/jp101482k
Published on Web 04/15/2010

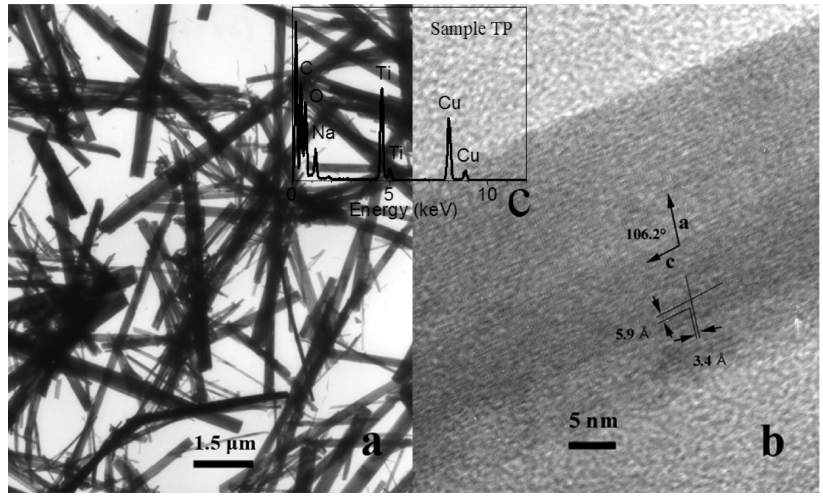

Figure 1. Sodium titanate nanobelts prepared from hydrothermal NaOH treatment on P25 (TiO_2) at 180 °C for 24 h: low-resolution TEM image of sample TP showing a lot of nanobelts (a), HRTEM image of a nanobelt of sample TP showing crystal lattices (b), and EDS spectrum of the nanobelt (c).

Characterization. The crystal structures of the synthesized products were identified by using XRD with a Philips X'Pert-MPD System with a Cu Kα radiation source ($\lambda = 0.154056$ nm). The size and shape of the products were determined by TEM images. TEM measurements were carried out on a HITACHI H-7500 (low-resolution) and a JEOL JEM2010 (high-resolution) transmission electron microscope. FE-SEM was performed on a JSM-6700F (JEOL, Japan). Energy-dispersive X-ray (EDX) spectroscopy for the elemental analysis of the sample was conducted on a JEOL JEM2010 TEM operated under an acceleration voltage of 200 kV. Thermogravimetric analysis (TGA)/differential thermal analysis (DTA) measurements were performed on a TGA 7 (PERKIN-ELMER, U.S.A) at a constant heating rate of 10 deg/min. The Raman spectra were recorded on a FRA 106/S Raman spectrometer (Bruker, Germany); a Nd/YAG laser (1064 nm) was used as an exciting light source.

Results and Discussion

Figure 1a shows typical TEM images of sample TP in the range of 60−370 nm in width and several micrometers in length. Each belt is straight due to its rigidness and has an unchanged width along its entire length. Figure 1b shows the HRTEM image of a nanobelt of sample TP. The lattice spacing of 0.59 and 0.34 nm with an angle around 106.2° can be resolved, respectively. On the basis of the result in Figure 1b, the sample TP is assumed as a sodium titanium oxide of $Na_2Ti_4O_9$ with space group $C2/m$ and lattice parameters $a = 17.38$ Å, $b = 3.784$ Å, $c = 11.99$ Å, and $\beta = 106.2°$ (JCPDS 33-1294), which is supported by its corresponding EDS measurement in Figure 1c. The atomic percents of Na, Ti, and O elements of the nanobelt are 12.64, 26.15, and 61.21, respectively, and the Ti/Na and O/Na atomic ratios are 2.069 and 4.842, respectively. The Ti/Na atomic ratio is very close to the theoretical atomic ratio of 2, while the O/Na atomic ratio is larger than the theoretical atomic ratio of 4.5, implying the existence of O element in the product as H_2O molecules. Thus, the exact chemical compositions of the as-synthesized sample can be formulated as $Na_2Ti_4O_9 \cdot xH_2O$. The x can be determined by TGA measurement (see below). The lattice spacing of 0.59 and 0.34 nm can be assigned to (300) and (004) planes. Their a and c axes are expanded about 1.8% and 13.4%, respectively, compared with that of $Na_2Ti_4O_9$. This may be ascribed to H_2O molecules inserted into interlayer spaces of layered $Na_2Ti_4O_9$.

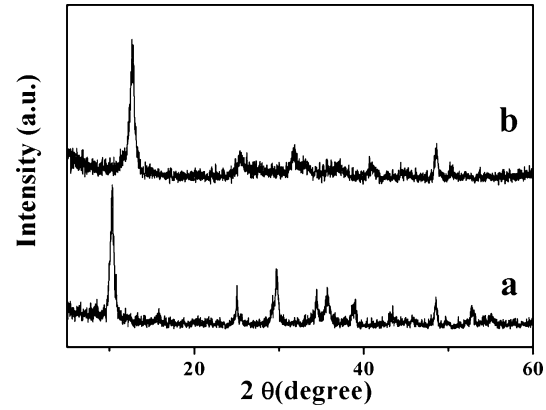

Figure 2. XRD patterns of as-synthesized sample and the sample calcined at 500 °C for 6 h: TP (a) and TP-500 (b).

Figure 2a shows the XRD pattern of sample TP, displaying a strong and narrow peak at 10.3° and other peaks at about 15.8°, 25.0°, 29.7°, 34.4°, 35.7°, 38.9°, 43.4°, 48.5°, and 52.7°. It is well-known that TiO_2 (P25) consists of 70% anatase and 30% rutile. The absence of any peaks from anatase or rutile means that the crystalline structure of P25 was completely broken during the hydrothermal treatment in concentrated aqueous NaOH solution at 180 °C for 24 h and formed into new crystalline material. Similar XRD patterns were found in the previous reports,[8,27] supporting further assignment of the sample TP to the composition with $Na_2Ti_4O_9$. To further investigate the thermal behavior of sample TP, TGA/DTA measurement was conducted and is shown in Figure 3. The TGA curve (Figure 3a) shows weight loss of about 10.5% from 50 to 500 °C and the corresponding DTA curve (Figure 3b) displays three endothermic peaks at about 100, 150, and 370 °C. The DTA curve does not show any exothermic peak, which indicates that the product is pure crystalline phase without any other amorphous phase. The weight percentage loss at 100 °C is about 1.3%, which is probably due to the removal of surface adsorbed water molecules. The second peak at about 150 °C is weight loss of 2.7%, which is probably due to the removal of water molecules bound to the surfaces of the sample. The remaining weight loss of 6.5% up to at 500 °C is probably due to the removal of water molecules confined in the interlayer spaces of as-synthesized product during the increase in temperature. The third peak at 370 °C is due to the phase transition.

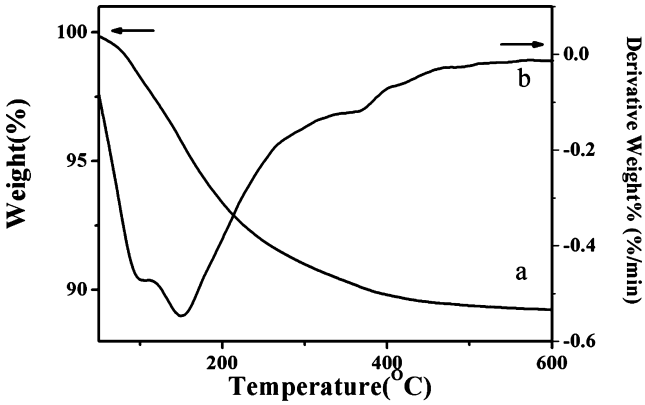

Figure 3. TGA curve (a) and DTA curve (b) of sample TP.

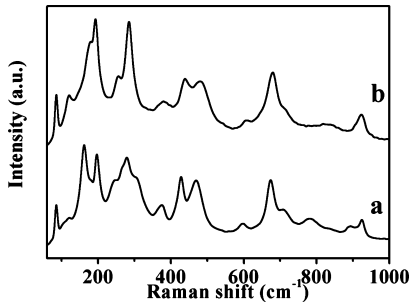

Figure 4. Raman spectra of as-synthesized sample, TP (a), and the sample calcined at 500 °C for 6 h, TP-500 (b).

According to the results mentioned above, we can conclude that as-synthesized TP is a hydrous sodium titanate nanobelt with $Na_2Ti_4O_9 \cdot 1.5H_2O$. The theoretical weight percent of water molecules of $Na_2Ti_4O_9 \cdot 1.5H_2O$ is 6.6%, close to the weight loss of 6.5% up to 500 °C determined by TGA measurement. The O/Na atomic ratio of $Na_2Ti_4O_9 \cdot 1.5H_2O$ is 5.25, larger than the 4.84 measurement of EDS, and this difference results from the removal of water molecules of the sample due to strong electron beam bombing under the condition of HRTEM.

To observe the thermal stability of the product, the sample TP was calcined at 500 °C for 6 h. The XRD pattern of TP-500 shown in Figure 2b still shows a strong and narrow peak but with a shift to the higher side at 12.6° and some other broad peaks at 25.4°, 31.6°, 36.8°, 40.7°, and 48.6°. It is found that after thermal treatment at 500 °C for 6 h, some peaks disappeared or became more broad and some new peaks appeared, indicating the occurrence of phase transition and lower crystallinity. Sample TP-500 can be assigned to $Na_2Ti_6O_{13}$, which displays the typical peaks at ca. 12°, 25° and 31° and has a base-centered monoclinic structure with a spatial group of $C2/m$ C_{2h}^3 ($a = 1.5120$ nm, $b = 0.3746$ nm, $c = 0.9162$ nm, $\beta = 99.28°$).[23,28] This assignment is further confirmed by Raman analysis (see below). According to TGA/DTA analysis above, the transition of $Na_2Ti_4O_9 \cdot 1.5H_2O$ to $Na_2Ti_6O_{13}$ occurred at 370 °C. On the basis of the reports,[17,23,24,29,30] some sodium titanates undergo the phase transition to $Na_2Ti_6O_{13}$ at different temperatures with increasing temperature, depending on the chemical composition and the methods used.

Figure 4 shows the Raman spectra of as-synthesized sample TP and sample TP-500. The Raman spectrum collected from the TP displays the peaks at about 84, 120, 161, 195, 246, 278, 306, 374, 426, 468, 597, 673, 708, 781, 893, and 923 cm^{-1}, as shown in Figure 4a. Except for bands at 84 and 120 cm^{-1},[8] this Raman spectrum is quite similar to that of $Na_2Ti_3O_7$, which were obtained by hydrothermal treatment of amorphous TiO_2 with

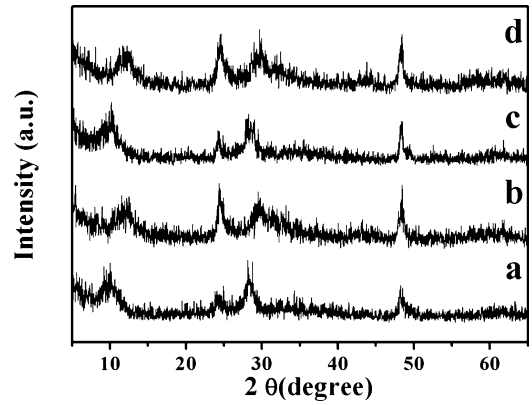

Figure 5. XRD patterns of various samples: TB (a), TB-500 (b), TC (c), and TC-500 (d).

NaOH solution at 200 °C for 20 h. This means that the Raman spectrum for $Na_2Ti_4O_9 \cdot 1.5H_2O$ is quite similar to that for $Na_2Ti_3O_7$. The Raman peaks at 161, 195, 278, and 306 cm^{-1} result from the Na−O−Ti stretching vibrations and the Raman peak at 923 cm^{-1} is assigned to the stretching vibration of terminal short Ti−O bonds involving nonbridging oxygen atoms that are coordinated with Na ions.[8,27] Figure 4b shows the Raman spectrum of sample TP-500. The Raman peaks at approximately 85, 121, 180, 192, 257, 284, 379, 439, 480, 607, 680, 715, and 923 cm^{-1} are quite close to those of $Na_2Ti_6O_{13}$, which was obtained by thermal treatment of $Na_2Ti_nO_{2n+1}$ ($n = 3$, 4, 9) at 500 °C for 10 h.[8] The exact assignment of the bands in the Raman spectrum is very difficult for $Na_2Ti_4O_9$ and $Na_2Ti_6O_{13}$ due to the lack of reports relating directly the Raman peaks to specific active modes of layered titanates.

To explore the dependence on the precursors, we also performed the synthesis of sodium titanates using $Ti(OBu)_4$ and $TiCl_4$ as the precursors. The XRD patterns of TB, TC, TB-500, and TC-500 are shown in Figure 5. The XRD patterns of TB and TC show similar and broad peaks at about 10.0°, 24.2°, 28.2°, 48.3°, and 61.8° (very weak), as shown in parts a and c of Figure 5, which are very close to those observed for $Na_2Ti_2O_4(OH)_2$.[31] The similarity of the XRD patterns of TB and TC indicates that the crystal structures of final products are independent of the precursors in these cases, although they are different from the XRD pattern of TP. After calcinations at 500 °C for 6 h, the XRD patterns of TB-500 and TC-500 shown in Figure 5b,d still show similar and broad peaks but with little shifts to higher positions at about 11.6°, 24.3°, 29.7°, 48.5°, and 61.8° (very weak). It is readily found that the peaks at 10.0° and 28.2° are shifted to higher position at 11.6° and 29.7°, while the peaks at 24.2°, 48.3°, and 61.8° are almost maintained. The shifts to higher positions suggest that the shrinkage of an axis of crystal structures of the TB and TC occurred during the calcination at 500 °C for 6 h, which is possibly due to the removal of water molecules from the products. This was confirmed by TGA measurements of TB and TC. TGA curves (Figure 6a,b) demonstrate a continuing mass loss of 12.6% and 10.8% from 50 °C up to 500 °C for TB and TC, respectively. The corresponding DTA curves (not shown) display endothermic peaks at about 111 and 101 °C for TB and TC, respectively, and the percentage weight losses at 111 and 101 °C for TB and TC are about 5.3% and 3.7%, respectively, which are probably due to the removal of water molecules bound to the surfaces of the samples. The remaining weight losses of 7.3% and 7.1% up to 500 °C for TB and TC, respectively, are probably due to the removal of water molecules confined in the interlayer spaces of as-synthesized product during the

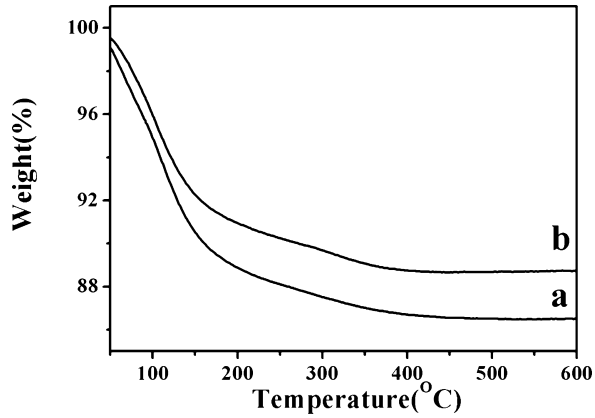

Figure 6. TGA results of TB (a) and TC (b).

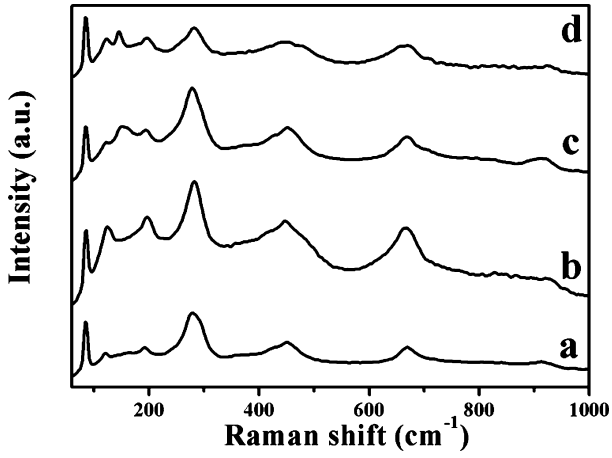

Figure 7. Raman spectra of as-synthesized samples and the samples calcined at 500 °C for 6 h: TB (a), TB-500 (b), TC (c), and TC-500 (d).

temperature increase. The Raman spectra of TB, TC, TB-500, and TC-500 are shown in Figure 7. The Raman spectra obtained from TB and TC (Figure 7a,c) display the peaks at about 84, 121, 192, 278, 450, 670, 910 cm^{-1} and 84, 123, 152, 194, 279, 451, 670, 915 cm^{-1}, respectively. The profiles of the Raman spectra of TB and TC are very similar to that of protonic lepidocrocite titanate ($H_xTi_{2-x/4}\square_{x/4}O_4$ ($x \approx 0.7$; □: vacancy)).[32] After calcinations at 500 °C for 6 h, the profiles of the Raman spectra of TB-500 and TC-500 (Figure 7b,d) are almost maintained but with little shifts to lower or higher positions.

The morphologies of TB and TC were also compared with TEM results. It is observed that thin nanobelts are split from the thick nanorods of TB, as evidenced in Figure 8. Figure 8a shows the TEM image of TB displaying a broom-like sodium titanate nanobelts splitting from a thick nanorod (width of ~240 nm).[8,12] Figure 8b shows the enlarged part of Figure 8a displaying a bundle of nanobelts with width of ~30 nm. Figure 8c shows the further enlarged part of Figure 8b displaying some nanobelts with widths of 16−34 nm. The lattice structure of a nanobelt is shown in Figure 9a and the corresponding SAED pattern is shown in Figure 9b. The lattice spacing along the direction of the nanobelt is 0.33 nm, while the lattice spacing perpendicular to the direction of the nanobelt is 0.82 nm, which are close to the reported results.[31,33] The SAED pattern (Figure 9b) shows a reflection characteristic of the nanobelt and the measured lattice spacing are consistent with that of Figure 9a. The FE-SEM image of TB (Figure 10) shows a large amount of nanobelt in the large scale. Most of them are flexible and curved. The lengths of the nanobelt are several micrometers and their widths are in the range of 14−22 nm. Figure 11a shows the TEM image of the sample TC showing a large amount of nanobelts of about 8 nm in width and over 100 nm in length. The corresponding SAED pattern is shown in Figure 11b. The lattice spacing corresponding to the four rings of the SAED pattern is 0.375, 0.194, 0.304, and 0.156 nm, respectively. The EDS spectrum over the nanobelts is shown in Figure 11c and Na elements are detected in the EDS spectrum. The widths of the three long nanorods shown in Figure 11d are 120, 300, and 450 nm, respectively, and their lengths are several micrometers. The SAED pattern of a nanorod with a width of 450 nm (Figure 11e) shows clearly many well-resolved spots, indicating good crystallinity of the nanorod. The lattice spacing corresponding to the four typical spots is 0.365, 0.192, 0.277, and 0.150 nm, respectively. Figure 12 shows FE-SEM images of sample TC. Figure 12a shows not only many dispersed nanorods but also many cotton-like blocks. Most of the nanorods are straight and their lengths are over 10 μm. Figure 12b shows the enlarged FE-SEM image of a cotton-like block showing a large amount of nanobelts. The widths of most of the nanobelts are about 10 nm. It is readily seen from Figure 12c that a nanorod is splitting into several nanorods, which is similar to the case shown in Figure 8. Figure 12d shows the enlarged image of the ends of the nanorods in Figure 12c.

On the basis of the results mentioned above, we can deduce the chemical composition of the sample TB and TC nanobelts. According to the XRD patterns, TGA data, and literature,[16,31–34] we can conclude that both samples TB and TC have the same chemical composition of $Na_2Ti_2O_4(OH)_2$ (orthorhombic unit cell with $a = 1.926$ nm, $b = 0.378$ nm, and $c = 0.300$ nm). The broad peaks at about $2\theta = 10.0°$, 24.2°, 28.2°, 48.3°, and 61.8° result from (200), (110), (600), (020), and (002) planes of $Na_2Ti_2O_4(OH)_2$. The structures of samples TB and TC were confirmed by TEM techniques. As shown in Figure 9, the lattice spacing of sample TB is 0.82 and 0.33 nm, which can be assigned to d_{200} and d_{010}, respectively. The lattice spacings of 0.375, 0.194, 0.304, and 0.156 nm from the SAED pattern shown in Figure 11b are in agreement with d_{010}, d_{020}, d_{001}, and d_{002}, respectively.[31] The lattice spacings of 0.365, 0.192, 0.277, and 0.150 nm measured from the four typical spots of SAED pattern shown in Figure 11e are close to d_{010}, d_{020}, d_{001}, and d_{002}, respectively. It should be noticed that some lattice spacings, such as 0.82 and 0.33 nm, are smaller than the theoretical values of $d_{200} = 0.963$ nm and $d_{010} = 0.378$ nm, respectively. It is well-known that sodium titanates may be dehydrated during microscopic observations due to the electron beam bombing on the samples and the high vacuum environment, leading to some shrinkage of the lattice constants. Thus, the lattice spacing measured from the HRTEM image and SAED pattern might not be accurate and are most likely to be decreased with the loss of hydrated water. As seen above, after calcination at 500 °C for 6 h, the peaks at 10.0° and 28.2° from the XRD patterns of samples TB and TC are shifted to higher positions at 11.6° and 29.7°, indicating the shrinkage of the a axis of crystal structures of samples TB and TC due to the removal of water molecules confined in the samples. We therefore consider that it is reasonable to index all of the measured lattice spacings to the corresponding reflection planes of $Na_2Ti_2O_4(OH)_2$.[31,33] This conclusion was also confirmed by TGA data. The water molecule weight losses of 7.3% and 7.1% from 111 and 101 °C up to at 500 °C for TB and TC, respectively, are close to the theoretical value of 7.5%.

Here we propose a crystalline structure model for $Na_2Ti_2O_4(OH)_2$, as shown in Figure 13. Figure 13a shows the

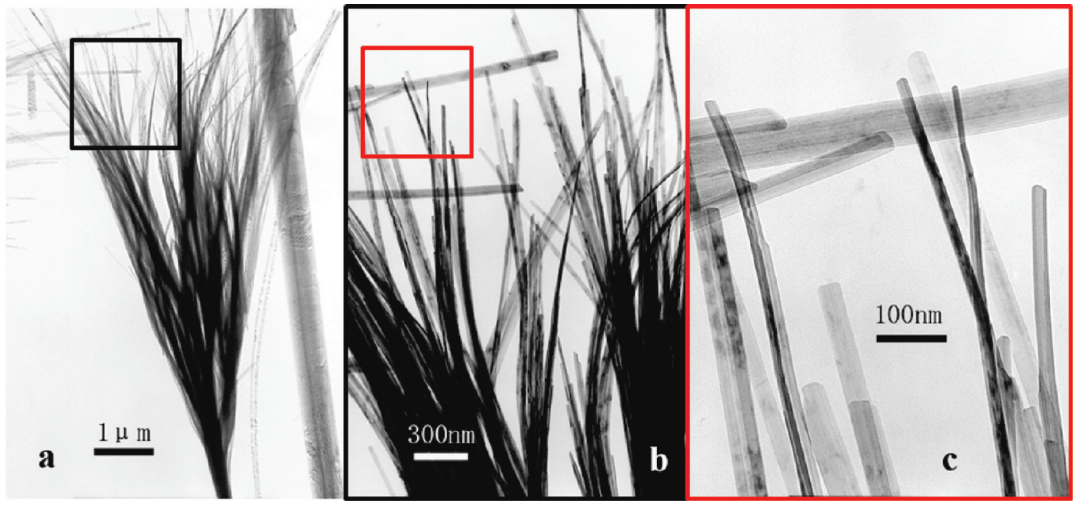

Figure 8. TEM images with different magnification of sample TB showing a bundle of sodium titanate nanobelts splitting from a thick nanorod: low magnification (a), medium magnification (b), and high magnification (c).

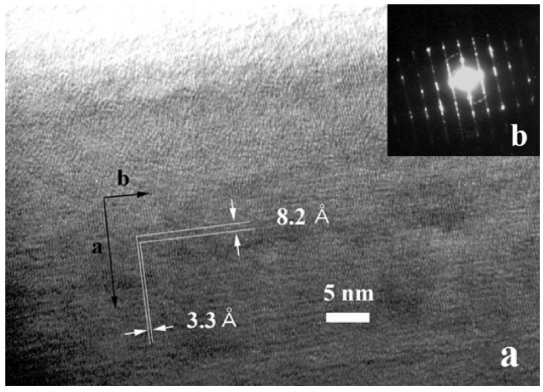

Figure 9. HRTEM image (a) and selected area electron diffraction pattern (b) of a nanobelt sample TB showing crystal lattice.

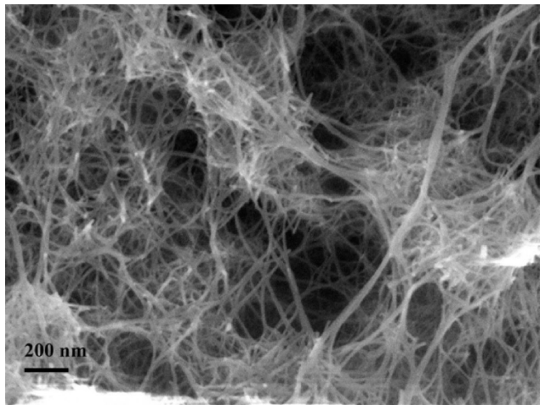

Figure 10. FE-SEM image of sample TB showing a large amount of nanobelts.

[001] projection of $Na_2Ti_2O_4(OH)_2$, showing the sides of [100] direction layers arrowed with numbers of 1−8 for discussions and the positions of O^{2-} (oxygen, red), Na^+ (sodium, blue), and H^+ (hydrogen, green) ions. Layer 1, layer 4, layer 5, and layer 8 are composed of O^{2-}, Na^+, and H^+ ions. The TiO_6 octahedra of layer 2 (yellow), layer 3 (orange), layer 6 (orange), and layer 7 (yellow) are edge-shared along the [010] direction, corner-shared along the [001] direction, and edge-shared with TiO_6 octahedra of the adjacent layer (e.g., layer 2 and layer 3, layer 6 and layer 7), as shown in Figure 13b,c. The O^{2-} ions occupy the valleys between corner-sharing TiO_6 octahedra of the layers (e.g., layer 2, layer 3, layer 6, and layer 7), as seen in Figure 13c, and bond with Na^+ and H^+ ions, forming a Na^+---O^{2-}--H^+ structure with a bonding angle larger than 90° (Figure 13d). The O^{2-} ion also interacts with its two neighboring Ti^{4+} ions of TiO_6 octahedra. Na^+ and H^+ ions of a layer (e.g., layer 4) are attracted not only by their four neighboring corner O^{2-} ions of TiO_6 octahedra but also by the O^{2-} ions of the adjacent layer (e.g., layer 5). Because of the repulsions between Na^+ and H^+ ions of two adjacent layers (e.g., layer 4 and layer 5), Na^+---O^{2-}--H^+ structures of layer 4 and layer 5 rotate by some degrees around their central axes cross the O^{2-} ions to part from each other to minimize the total energy of the crystal system, as shown in Figure 13b. For clarity, the [100] projections of the Na^+---O^{2-}--H^+ structure of layer 4 and layer 5 are separately shown in Figure 13b, as indicated by arrow 4 and arrow 5, respectively.

On the basis of the observations above and the crystalline structure model for $Na_2Ti_2O_4(OH)_2$, we can propose a formation mechanism of sample TB and TC nanobelts. The intermediates containing Ti−O−Na and Ti−OH are initially formed upon adding precursors into aqueous NaOH solution. During the hydrothermal treatment, these intermediates further react with each other to form atomic layers (e.g., layer 2 and layer 3) with the edge-sharing TiO_6 octahedra along the [010] direction and the corner-sharing TiO_6 octahedra along the [001] direction. These two atomic layers further react to form double-layer by edge-sharing TiO_6 octahedra (see Figure 13b). After that, multilayers are formed through the interactions between double-layers adsorbed with Na^+, H^+, and O^{2-} ions on their surfaces, which leads to a layer-by-layer growth of $Na_2Ti_2O_4(OH)_2$. The driving force of bonding the double-layers is a dipole−dipole interaction between double-layers containing Na^+, H^+, and O^{2-} ions, i.e., Na^+, H^+, and O^{2-} ions act as the adhesive between the double-layers. The growth rate of $Na_2Ti_2O_4(OH)_2$ along the [010] and [001] directions should be faster than that along the [100] direction due to a stronger chemical bonding of the [010] and [001] directions compared to that of the [100] direction, forming a thin layer with (100) planes as the top/bottom surfaces. As a result, $Na_2Ti_2O_4(OH)_2$ structures with (100) planes as top/bottom surfaces should be observed. However, this structure was not observed in this work, as shown in Figure 9a. This

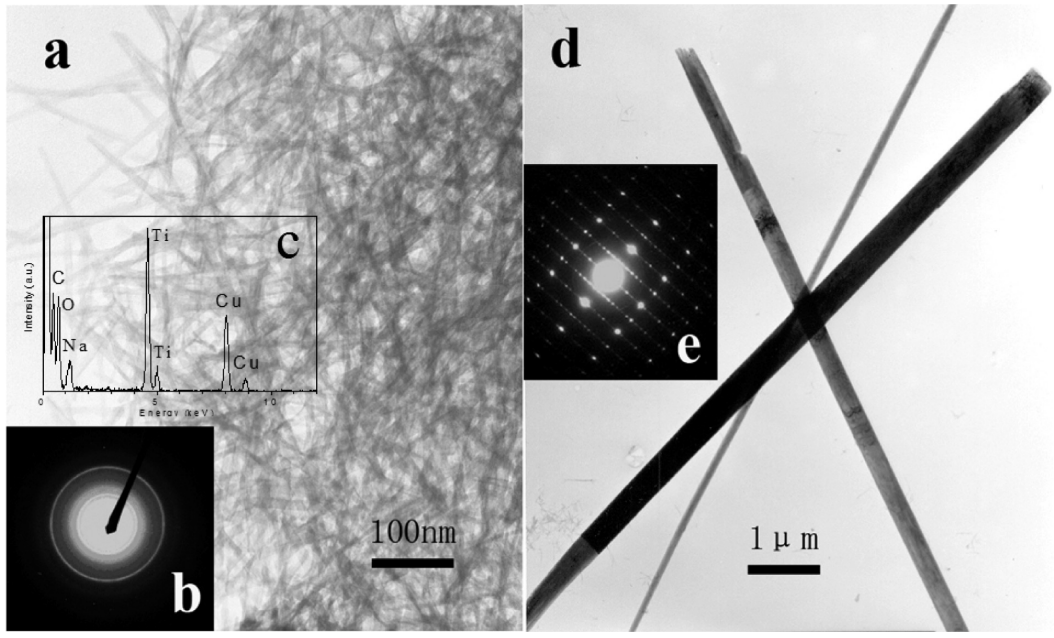

Figure 11. (a) TEM image of sample TC showing a large amount of nanobelts, (b) selected area electron diffraction pattern of panel a, (c) EDS spectrum of the nanobelts of panel a, (d) TEM image of sample TC showing three very long nanorods with different diameters, and (e) selected area electron diffraction pattern of the largest diameter of the nanorods of panel d.

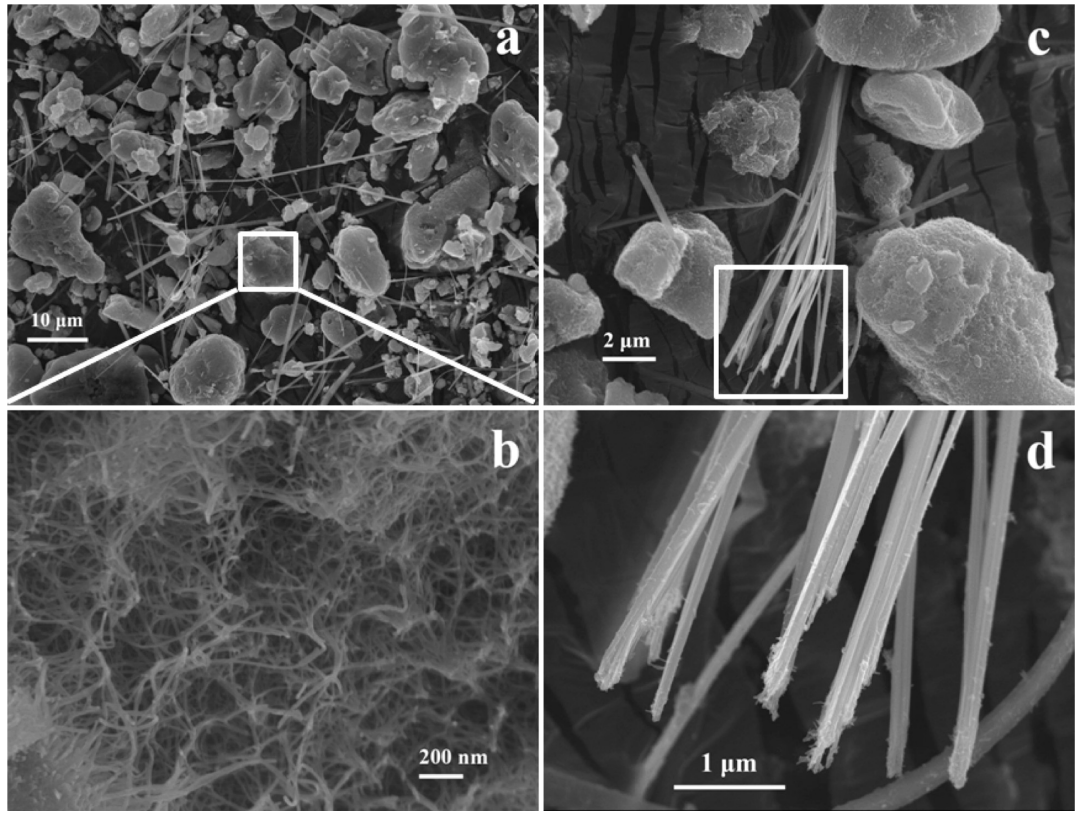

Figure 12. FE-SEM images of sample TC: (a) low-magnification image showing many cotton-like blocks and many long nanorods, (b) high-magnification image of a cotton-like block of panel b, showing a large amount of nanwires, (c) a thick nanorod splitting into several long nanorods, and (d) a detail image of the ends of several nanorods of panel c.

phenomenon can be explained through the following formation mechanism for $Na_2Ti_2O_4(OH)_2$ nanobelts. A schematic diagram of the formation process for $Na_2Ti_2O_4(OH)_2$ nanobelts is depicted in Figure 14. During the cooling process after hydrothermal reaction, the bulk $Na_2Ti_2O_4(OH)_2$ structures may split not only between (100) planes (e.g., layer 4 and layer 5) due to weaker chemical bonding but also between (001) planes due to internal stress probably resulting from the structure feature of edge-sharing TiO_6 octahedra. This internal stress is probably proportional to the width of the product along the [001] direction. As a result, the products are split into thick rods a few micrometers in width with a rectangular cross section of

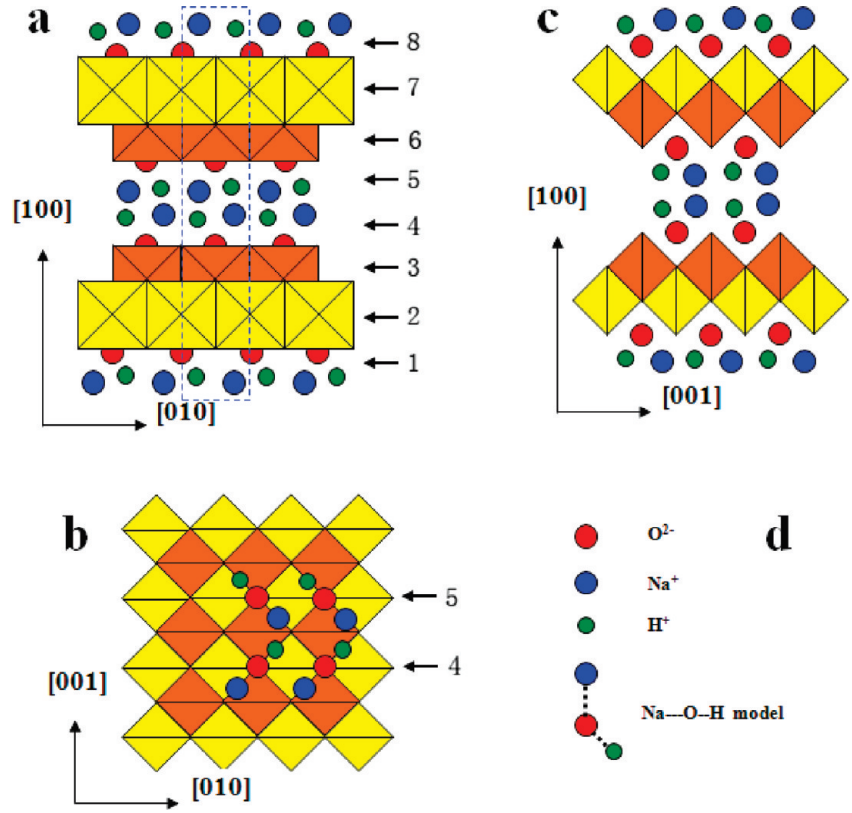

Figure 13. Proposed crystal structure model for $Na_2Ti_2O_4(OH)_2$: (a) projection along the [001] direction, showing a unit-cell structure closed by a blue dotted line, (b) projection along the [100] direction, (c) projection along the [010] direction, and (d) three symbols of O^{2-} (red), Na^+ (blue), and H^+ (green) ions and the Na---O--H model.

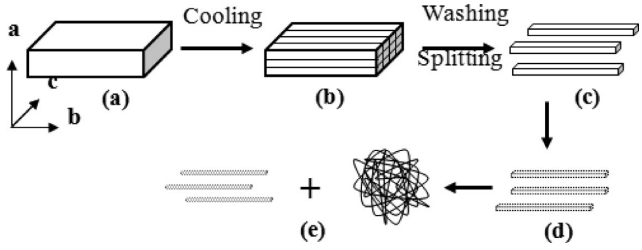

Figure 14. Schematic diagram of the formation process for $Na_2Ti_2O_4(OH)_2$ nanobelts: (a) $Na_2Ti_2O_4(OH)_2$ product, (b) $Na_2Ti_2O_4(OH)_2$ product with cracks on its surface along the [010] direction after cooling, (c) thick rods split from the product along the [010] direction during water washing, (d) nanorods split from the thick rods along the [010] direction during water washing, and (e) a cotton-like block aggregated with the nanobelts exfoliated from the nanorods and thinner nanorods remaining after the exfoliation of the nanorods during water washing.

two (100) planes and two (001) planes as their four side surfaces, but all contact with each other after cooling (Figure 14b). During the water washing process, the thick rods are completely separated from each other (Figure 14c) and start from the ends of the thick rods to be split further into many nanorods (Figure 14d) with rectangular cross sections. Some of the nanorods display the (001) planes as top/bottom surfaces, as evidenced in Figure 9a. Due to the disappearance of (001) plane stress with the decease of the nanorod widths along the [001] directrion, the nanobelts with (100) planes start to be exfoliated from the nanorods with the decrease in pH value of the washing solution. The exfoliated nanobelts are further aggregated into many cotton-like blocks by van der Waals forces between them, and some thinner nanorods remain (Figure 14e). This mechanism explanation also can be confirmed by the phenomena that appeared during the water washing process. With the decrease in pH from higher than 14 to 14, the white precipitates appeared immediately at the bottom of the flask after water washing. With a further decrease in pH from 14 to 9, the washing solution became turbid and some white precipitates were also found at the bottom of the flask. These facts suggested that the initially appearing white precipitates were probably thick rods that split into nanorods until pH 14, and then large amounts of nanobelts were gradually exfoliated from the nanorods with a further decrease in pH from 14 to 9, as indicated by the appearance of turbidity in the washing solution, and some thinner nanorods remained at pH 9.

Conclusions

In this study, sodium titanate nanobelts were synthesized by means of the hydrothermal method, using three different precursors in the concentrated aqueous NaOH solution as the solvents. The product obtained with P25 (TiO_2) was identified to be $Na_2Ti_4O_9 \cdot 1.5H_2O$. The product prepared with $Ti(OBu)_4$ and $TiCl_4$ was confirmed to have the crystalline structure of $Na_2Ti_2O_4(OH)_2$. This means that the formation mechanism of the crystalline structure of sodium titanate synthesized with TiO_2 as a source is different from that of sodium titanate synthesized with other materials as the sources. The proposed crystalline structure model for $Na_2Ti_2O_4(OH)_2$ has the unique feature of the separation of positive and negative charges along the [100] direction. Therefore, if this model is correct, this type of nanomaterial can be used as another candidate for applications in related fields, such as the piezoelectricity field. Further investigations are needed to reveal the properties of $Na_2Ti_2O_4(OH)_2$.

Acknowledgment. This work was supported by Basic Science Research Program through the National Research Foundation of Korea (NRF) grant funded from the Ministry of Education, Science and Technology (MEST) of Korea for the Center for Next Generation Dye-sensitized Solar Cells (No. 2010-0001842). C.W.K. acknowledges the financial support by the Brain Korea 21 in 2010.

References and Notes

(1) Kasuga, T.; Hiramatsu, M.; Hoson, A.; Sekino, T.; Niihara, K. *Langmuir* **1998**, *14*, 3160.
(2) Gao, X.; Zhu, H.; Pan, G.; Ye, S.; Lan, Y.; Feng Wu, F.; Song, D. *J. Phys. Chem. B* **2004**, *108*, 2868.
(3) Rabatic, B. M.; Dimitrijevic, N. M.; Cook, R. E.; Saponjic, Z. V.; Rajh, T. *Adv. Mater.* **2006**, *18*, 1033.
(4) Kasuga, T.; Hiramatsu, M.; Hoson, A.; Sekino, T.; Niihara, K. *Adv. Mater.* **1999**, *11*, 1307.
(5) Du, G. H.; Chen, Q.; Che, R. C.; Yuan, Z. Y.; Peng, L. M. *Appl. Phys. Lett.* **2001**, *79*, 3702.
(6) Yao, B. D.; Chan, Y. F.; Zhang, X. Y.; Zhang, W. F.; Yang, Z. Y.; Wang, N. *Appl. Phys. Lett.* **2003**, *82*, 281.
(7) Zhu, H.; Gao, X.; Lan, Y.; Song, D.; Xi, Y.; Zhao, J. *J. Am. Chem. Soc.* **2004**, *126*, 8380.
(8) Kolen'ko, Y. V.; Kovnir, K. A.; Gavrilov, A. I.; Garshev, A. V.; Frantti, J.; Lebedev, O. I.; Churagulov, B. R.; Tendeloo, G. V.; Yoshimura, M. *J. Phys. Chem. B* **2006**, *110*, 4030.
(9) Yang, H. G.; Zeng, H. C. *J. Am. Chem. Soc.* **2005**, *127*, 270.
(10) Sun, X.; Chen, X.; Li, Y. *Inorg. Chem.* **2002**, *41*, 4996.
(11) Xu, C. Y.; Zhang, Q.; Zhang, H.; Zhen, L.; Tang, J.; Qin, L. C. *J. Am. Chem. Soc.* **2005**, *127*, 11584.
(12) Wu, D.; Liu, J.; Zhao, X.; Li, A.; Chen, Y.; Ming, N. *Chem. Mater.* **2006**, *18*, 547.
(13) Li, J.; Tang, Z.; Zhang, Z. *Chem. Mater.* **2005**, *17*, 5848.
(14) Chen, Q.; Zhou, W.; Du, G.; Peng, L. M. *Adv. Mater.* **2002**, *14*, 1208.
(15) Ma, R.; Sasaki, T.; Bando, Y. *J. Am. Chem. Soc.* **2004**, *126*, 10382.
(16) Ma, R.; Bando, Y.; Sasaki, T. *Chem. Phys. Lett.* **2003**, *380*, 577.
(17) Sun, X.; Li, Y. *Chem.—Eur. J.* **2003**, *9*, 2229.
(18) Nosaka, A. Y.; Nishino, J.; Fujiwara, T.; Ikegami, T.; Yagi, H.; Akutsu, H.; Nosaka, Y. *J. Phys. Chem. B* **2006**, *110*, 8380.
(19) Jiu, J.; Isoda, S.; Wang, F.; Adachi, M. *J. Phys. Chem. B* **2006**, *110*, 2087.
(20) Wang, G.; Wang, Q.; Lu, W.; Li, J. *J. Phys. Chem. B* **2006**, *110*, 22029.
(21) Mao, Y.; Kanungo, M.; Hemraj-Benny, T.; Wong, S. S. *J. Phys. Chem. B* **2006**, *110*, 702.
(22) Wang, X. D.; Jin, Z. S.; Pei, X. R.; Yang, J. J.; Zhang, Z. J. *Chin. Chem. Lett.* **2006**, *17*, 1275.
(23) Štengl, V.; Bakardjieva, S.; Šubrt, J.; Večerníková, E.; Szatmary, L.; Klementová, M.; Balek, V. *Appl. Catal., B* **2006**, *63*, 20.
(24) Zhao, Y.; Lee, U. H.; Suh, M.; Kwon, Y. U. *Bull. Korean Chem. Soc.* **2004**, *25*, 1341.
(25) Zang, H.; Cheng, K.; Ji, Y. L.; Liu, X. L.; Li, L. S.; Zhang, X. T.; Du, Z. L. *Sci. China, Ser B: Chem.* **2008**, *51*, 976.
(26) Inoue, Y.; Kubokawa, T.; Sato, K. *J. Phys. Chem.* **1991**, *95*, 4059.
(27) Yada, M.; Inoue, Y.; Uota, M.; Torikai, T.; Watari, T.; Noda, I.; Hotokebuchi, T. *Langmuir* **2007**, *23*, 2815.
(28) Ramirez-Salgado, J.; Djurado, E.; Fabry, P. *J. Eur. Ceram. Soc.* **2004**, *24*, 2477.
(29) Papp, S.; Korosi, L.; Meynen, V.; Cool, P.; Vansant, E. F.; Dekany, I. *J. Solid State Chem.* **2005**, *178*, 1614.
(30) Viana, B. C.; Ferreira, O. P.; Filho, A. G. S.; Filho, J. M.; Alves, O. L. *J. Braz. Chem. Soc.* **2009**, *20*, 167.
(31) Yang, J.; Jin, Z.; Wang, X.; Li, W.; Zhang, J.; Zhang, S.; Guo, X.; Zhang, Z. *Dalton Trans.* **2003**, 3898.
(32) Mao, Y.; Wong, S. S. *J. Am. Chem. Soc.* **2006**, *128*, 8217.
(33) Tsai, C. C.; Teng, H. *Chem. Mater.* **2006**, *18*, 367.
(34) Gao, T.; Fjeld, H.; Fjellvag, H.; Norby, T.; Norby, P. *Energy Environ. Sci.* **2009**, *2*, 517.

JP101482K